



PCCP

**The Role of Cations in Uranyl Nanocluster Association: A
Molecular Dynamics Study**

Journal:	<i>Physical Chemistry Chemical Physics</i>
Manuscript ID	CP-ART-09-2019-005138.R1
Article Type:	Paper
Date Submitted by the Author:	02-Dec-2019
Complete List of Authors:	Newcomb, Ken; University of Notre Dame, Chemical and Biomolecular Engineering Bernales, Varinia; University of Minnesota, Department of Chemistry and Supercomputing Institute Tiwari, Surya; University of Notre Dame, Chemical and Biomolecular Engineering Gagliardi, Laura; University of Minnesota, Department of Chemistry and Supercomputing Institute Maginn, Edward; University of Notre Dame, Chemical and Biomolecular Engineering

SCHOLARONE™
Manuscripts

Cite this: DOI: 00.0000/xxxxxxxxxx

The Role of Cations in Uranyl Nanocluster Association: A Molecular Dynamics Study[†]

Ken Newcomb^a, Varinia Bernales^b, Surya Prakash Tiwari^a, Laura Gagliardi^b, and Edward J. Maginn^a

Received Date

Accepted Date

DOI: 00.0000/xxxxxxxxxx

Actinyl ions can self-assemble in aqueous solution to form closed cage clusters ranging from 1.5 to 4.0 nm in diameter. The self-assembly, stability, and behavior of the nanoclusters depend on the nature of the aqueous environment, such as the pH and cations present. In this work, a classical force field for $[(\text{UO}_2)_{20}(\text{O}_2)_{30}]^{20-}$ (U_{20}) peroxide nanoclusters in aqueous solution was developed from quantum-mechanical calculations. Using molecular dynamics simulations, the preferred binding sites of six cations (Li^+ , Na^+ , K^+ , Rb^+ , Cs^+ , and Ca^{2+}) to the nanocluster were determined. Replica exchange molecular dynamics was used to equilibrate the structure and determine the equilibrium distribution of cations and water with respect to the nanocluster cage. In addition, the free energy barriers associated with cations entering the cluster were computed. Finally, the association of two cages was investigated by computing the free energy as a function of intercage distance. The free energy profiles reveal that the nanoclusters prefer to be associated when neutralized with divalent cations, but do not associate when neutralized with monovalent cations. This could explain the formation of tertiary structures observed experimentally.

1 Introduction

Burns et al. have synthesized over 60 nanoscale uranyl peroxide clusters (also called nanoclusters or cage clusters) to date¹. The nanoclusters are formed from the self-assembly of 20–124 uranyl ions in aqueous solution, with diameters ranging from 1.5 to 4.0 nm. Each nanocluster has a distinct topology, with uranyl groups coordinated by four, five or six ligands by arranging at the equatorial vertices of square, pentagonal, or hexagonal bipyramids. Ligands vary from O_2^{2-} , OH^- , H_2O , silicate, sulfate, phosphate, and carbonate^{2–5}. The nanoclusters carry an overall negative charge ranging from -20 to -60, which is balanced by cations in solution. Nanoclusters have a promising future in designing advanced nuclear cycles², in which actinides will form nanoclusters in the aqueous phase and can be simply filtered out due to their size, thus avoiding the usage of any liquid-liquid extraction processes. This technology could considerably reduce the amount of nuclear waste for final disposal.

The nanoclusters can further assemble into tertiary struc-

tures. Burns et al. recently used cryo-TEM to study $[(\text{UO}_2(\text{O}_2)\text{OH})_{60}]^{60-}$ (U_{60}) nanoclusters in the presence of mono- and divalent cations⁶. When neutralized with divalent cations (Ca^{2+}), the nanoclusters aggregate into spherical macroassemblies known as “blackberries”, consisting of hundreds of individual nanoclusters. However, in the presence of monovalent cations (K^+), the nanoclusters form elongated structures. The exact role of the cations in this process is not well understood experimentally. Molecular simulation can elucidate the role of the cations by providing atomic-level resolution of the process. In addition, thermophysical properties like free energies, stability constants, and diffusivities can be determined from the simulations^{7,8}.

Miró et al.⁹ developed the first force field parameters for the simulation of uranyl peroxide and its nanoclusters in water. They parameterized a classical force field by computing interaction energies via second order Møller-Plesset perturbation theory calculations. Using classical molecular dynamics (MD), they studied the $[(\text{UO}_2)_{20}(\text{O}_2)_{30}]^{20-}$ nanocluster (hereafter referred to as the U_{20} nanocluster) in water and predicted an ice-like structure of water within the nanocluster. They also studied the cluster in the presence of Na^+ cations, and reported the disruption of the inner structure when a cation enters. However, due to slow dynamics, they were only able to see a single Na^+ enter the nanocluster, which we will demonstrate is not the equilibrium structure. Peruski et al.¹⁰ performed MD simulations on the U_{60} nan-

^a Department of Chemical and Biomolecular Engineering, 250 Nieuwland Hall, University of Notre Dame, Notre Dame, IN 46556, USA. E-mail: ed@nd.edu;

Fax: +1 574 631 8366; Tel: +1 574 631 5687

^b Department of Chemistry, Minnesota Supercomputing Institute, University of Minnesota, Minneapolis, Minnesota 55455, USA.

[†] Electronic Supplementary Information (ESI) available: [details of any supplementary information available should be included here]. See DOI: 00.0000/00000000.

occur to determine the preferred binding locations of cations. They modeled the cluster as a rigid body, and used the Universal Force Field with the Extended Simple Point Charge¹¹ (SPC/E) water model to describe the intermolecular interactions. Relatively short 1 ns simulations were used to compute coordination number (CN) statistics, which may be problematic if the cations have to surmount large free energy barriers to enter the cluster.

The goal of the present work is to accurately determine the binding sites of water and various cations (Li^+ , Na^+ , K^+ , Rb^+ , Cs^+ , and Ca^{2+}) to the U_{20} nanocluster, and to better understand how the identity of the cation affects nanocluster aggregation. In this paper, we utilize a new classical force field¹² for the simulation of U_{20} nanoclusters in SPC/E water using a combination of Lennard-Jones (LJ) and Coulomb potentials. Classical MD was used to determine the preferred binding sites of the cations. Replica exchange molecular dynamics (REMD) was used to ensure equilibration and ultimately determine the equilibrium distribution of cations and water around the nanocluster. In addition, the free energy barrier associated with a cation entering the nanocluster was computed. Finally, the association of two U_{20} nanoclusters was explored by free energy calculations. The free energy of association was found to vary greatly with the valency of the charge balancing cations.

2 Methods

2.1 The U_{20} Nanocluster

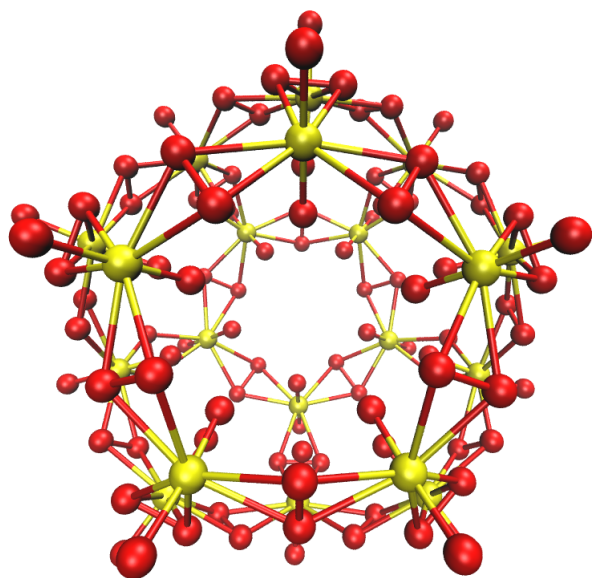


Fig. 1 U_{20} nanocluster. Uranium and oxygen atoms are colored yellow and red, respectively.

The U_{20} nanocluster is one of the smallest uranyl nanoclusters that has been synthesized¹³, with a diameter of 1.5 nm. It is formed through the self assembly of UO_2^{2+} groups in aqueous solution, bridged together by peroxides. Small charge-balancing cations, along with water, can move in and out of the cluster through one of the 12 hexagonal faces, shown in Figure 1. The precise locations of the cations have not been determined experimentally.

2.2 $\text{U}_{20}\text{-H}_2\text{O}$ Force Field Parameterization

Due to the large size of the U_{20} , QM energy calculations on the cluster are prohibitively expensive. Therefore, the LJ parameters were derived from QM calculations on a smaller, representative peroxide system, $(\text{UO}_2)_2(\text{O}_2)^{2+}$ (U_2O_6). This subunit is shown in Figure 2.

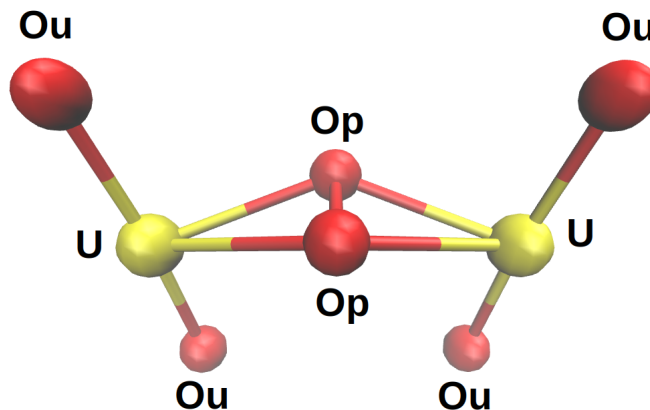


Fig. 2 U_2O_6 peroxide subunit.

Force field parameters were obtained by fitting interaction energy curves generated between U_2O_6 and a single water molecule. Interaction energies were computed using second-order Møller-Plesset perturbation theory (MP2) as implemented in the Molcas 7.8 package¹⁴. Uranyl peroxide geometries were taken from ref. 9, while the geometry of the interacting water molecule was adapted to SPC/E model geometric constraints.¹¹ Counterpoise correction was included in the MP2 calculations to account for the basis set superposition error and relativistic effects were included using the scalar Douglas-Kroll-Hess Hamiltonian. An ANO-RCC-VTZP basis set was used for all atoms.^{15–18} Additionally, the Cholesky decomposition technique was combined with local exchange screening to significantly reduce the computational cost involved in generating the two-electron integrals.¹⁹

Previous studies on the uranyl nanocluster by Miró et al.⁹ computed charges from the smaller peroxide system and applied them to the simulation of the uranyl nanocluster. In our work, CM5 partial atomic charges were obtained from a single point calculation performed on the full U_{20} nanocluster with the LC- ω PBE density functional^{20–22} as implemented in the Gaussian 09 software.²³ Regarding basis sets, the Stuttgart small-core scalar-relativistic pseudopotential was used to describe the 60 core electrons in uranium atoms, while the remaining 32 electrons were represented by the ECP60MWB-SEG associated valence basis set.^{24–26} The aug-cc-pvtz basis set was used to describe oxygen atoms.^{27,28} Ultrafine grids were used in the numerical integration of the exchange-correlation portion of the density functional. Bulk aqueous solvent effects were introduced using the SMD continuum solvation model.²⁹ CM5 charges were obtained by using the cm5pac package.^{30,31}

The force field used in this study consists of a combination of the Lennard-Jones (LJ) and Coulomb potentials:

$$U_{total} = \sum_{i,j} \left[4\epsilon_{ij} \left(\left(\frac{\sigma_{ij}}{r_{ij}} \right)^{12} - \left(\frac{\sigma_{ij}}{r_{ij}} \right)^6 \right) + \frac{q_i q_j}{4\pi\epsilon_0 r_{ij}} \right] \quad (1)$$

where r_{ij} , σ_{ij} , ϵ_{ij} , q_i , q_j , and ϵ_0 are the separation between two interacting sites, LJ atomic diameter, LJ energy well depth, partial atomic charges on sites i and j , and the permittivity of vacuum, respectively. All species were treated as rigid bodies. Previous simulations on actinyl nanoclusters⁹ incorporated a Born-Huggins-Meyer (BHM) potential. We chose to use a combined LJ and Coulomb model for a couple of reasons. We wanted to derive a force field that was compatible with popular water models. Using the Lorentz-Berthelot mixing rules³², our force field can be easily extended to many water models (SPC, SPC/E, TIP3P, TIP4P, etc.), as well as other solvents. In addition, we previously had success modeling uranyl cations in water using the LJ potential^{7,8,33} so it was a natural choice for the nanocluster system.

First, charges on the U_2O_6 were set to the values determined from the CM5 calculations, discussed previously. The partial charges on water were set to the SPC/E model. The LJ parameters of uranium (U) and the uranyl oxygen (Ou) were set to the values derived for uranyl ions in our previous work³³. The two LJ parameters corresponding to the interaction between the peroxide oxygen of the U_2O_6 (Op) and the oxygen of water (Ow) were fit to the energies from the MP2 calculations described above. Six different U_2O_6 -H₂O arrangements were used in the fits, and the energies are shown in Figure 3 as a function of distance. The lower energy curves were weighed more heavily than the higher energy curves, since these states are more likely to be sampled. The QM potential energy surfaces (PES), along with the force field fits, are shown in Figure 3b. The LJ parameters derived from the fitting process and the atomic charges computed from CM5 are shown in Table 1, along with other parameters taken from the literature.

Table 1 Force Field Parameters for U_{20} -H₂O used in this work

Atom Type	σ_{ii} (nm)	ϵ_{ii} (kJ/mol)	q_i (e)	Reference
U_{20}				
U	0.295	0.530	2.138	33
Ou	0.383	0.057	-0.829	33
Op	0.267	1.538	-0.494	This work
Water				
Ow	0.3166	0.650	-0.840	11
Hw	0.0	0.0	0.420	11
Cations				
Li ⁺	0.1582	1.409	1.0	34
Na ⁺	0.2160	1.475	1.0	34
K ⁺	0.2839	1.798	1.0	34
Rb ⁺	0.3096	1.862	1.0	34
Cs ⁺	0.3603	0.376	1.0	34
Ca ²⁺	0.2410	0.940	2.0	35

2.3 MD Simulations

GROMACS 2016.3³⁶ was used for all MD simulations. Simulations were first performed on the uranyl peroxide subunit, to verify the accuracy of the derived force field. The radial distribution functions match both experiment and previous simulation studies, and can be found in the Supplementary Information (SI). Single nanocluster simulations consisted of one U_{20} nanocluster, 2048 SPC/E water molecules, and either 10 divalent cations or 20 monovalent cations in a cubic simulation volume. Periodic boundary conditions were incorporated in all three directions. Long-range electrostatic forces were handled using particle-mesh Ewald (PME). A switch function was used for the LJ interactions, which is turned on at 1.1 nm to make the force smoothly go to zero at a distance of 1.2 nm. Non-bonded interactions were excluded for atoms connected by at most 3 bonds. MD simulations were carried out in the *NVT* ensemble using the density computed from a 20 ns *NPT* simulation at 1 atm and 298 K. The production run consisted of a 100 ns simulation, with a 1 fs timestep. To study the association of two nanoclusters, a similar simulation protocol was used. For these simulations, two U_{20} nanoclusters and 10,000 SPC/E water molecules were used, along with sufficient monovalent or divalent cations to neutralize the system. Note that the U_{20} Cartesian coordinates were obtained from Ref. 9.

Replica exchange molecular dynamics (REMD) was used to further equilibrate the system. REMD is a widely used³⁷⁻³⁹ enhanced sampling method that consists of running independent replicas of the system at various temperatures and swapping adjacent configurations at regular intervals. This allows the system to efficiently escape energy minima, as important unsampled states flow down from the higher temperature simulations. The probability of swapping two adjacent configurations, i and j , is given by:

$$p_{ij} = \min\left(1, e^{\left(\frac{1}{k_B T_i} - \frac{1}{k_B T_j}\right)(E_i - E_j)}\right) \quad (2)$$

where k_B is the Boltzmann constant, T is the absolute temperature, and E is the total energy. This acceptance rule ensures that proper canonical ensemble probabilities are obtained at the temperature of interest, 298K. For our REMD simulations, 40 simulation windows from 298K to 500K were used. Exchanges were attempted every 10,000 steps. Total energy histograms were generated at each temperature to ensure good overlap between adjacent windows. More details can be found in the SI.

We also wished to compute the free energy with respect to two reaction coordinates: U_{20} -cation distance and U_{20} - U_{20} distance. The potential of mean force (PMF), $W(r)$, gives the free energy change along some reaction coordinate r . In theory, it can be computed from the radial distribution function, $g(r)$:

$$W(r) = -k_B T \ln[g(r)] + C \quad (3)$$

where C is an arbitrary constant. However, the calculation of $W(r)$ from a standard MD simulation is often impractical, since the presence of large energy barriers along r may prevent an accurate sampling of the configurational space within the available

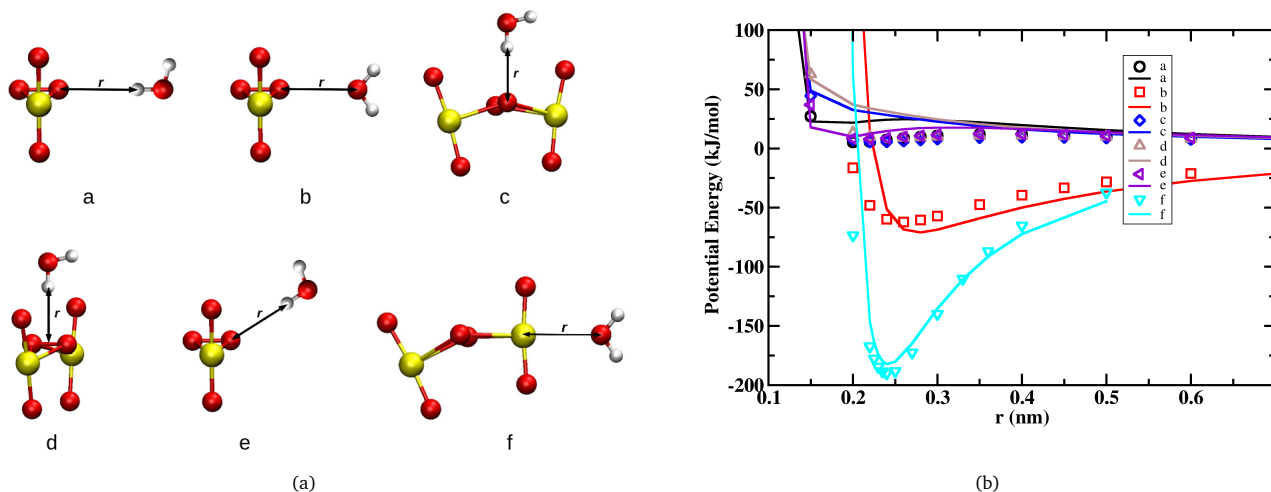


Fig. 3 Different configurations (a) and corresponding QM PESs along with force field fits to derive the parameters for $[(\text{UO}_2)_2\text{O}_2]^{2+}$ -water interactions (b). QM energies are shown as symbols, and the force field fits are shown as lines.

computer time.⁴⁰ To overcome this limitation, we used the adaptive biasing force (ABF) algorithm, a rapidly convergent free energy method.⁴¹ ABF accrues a running estimate of the average force between the two species of interest, and applies an equal and opposite biasing force. This average force \bar{F} is equal to the derivative of the Helmholtz free energy, $A(r)$:

$$\bar{F} = \frac{d}{dr}A(r; N, V, T) \quad (4)$$

All free energy calculations were performed using the SSAGES simulation suite.⁴² 300 histogram bins were used to store the average force along r . The average force in each bin was turned on using a linear ramp over 50,000 histogram counts to avoid instability.

3 Results

3.1 Radial distribution functions

We first sought to understand the distribution of cations and water within and around the nanocluster by computing radial distribution functions (RDFs). The RDF is computed with respect to r , the distance between the U_{20} center of mass and the cation. The U_{20} -water RDFs for the monovalent cation systems can be split into two groups. The two lightest alkali metals, Li^+ and Na^+ , comprise the first group. Their RDFs, shown in Figure 4a, has three peaks. The first peak, located at $r = 0.25$ nm, corresponds to a highly localized population of cations inside the cage. The second peak, at approximately $r = 0.65$ nm, corresponds to cations that sit on one of the 12 pentagonal faces of the cluster. The final population of cations can be found between $r = 0.75$ nm and $r = 1.25$ nm, and is shown in the figure inset. K^+ , Rb^+ , and Cs^+ comprise the second group of monovalent cations. The RDFs corresponding to second group (Figure 4b) show two additional peaks. There is a peak at $r = 0.45$ nm that corresponds to a second population of cations inside of the cage, as well a layer

of cations at $r = 0.91$ nm, which is more localized than the outer population of cations observed in the case of Li^+ and Na^+ .

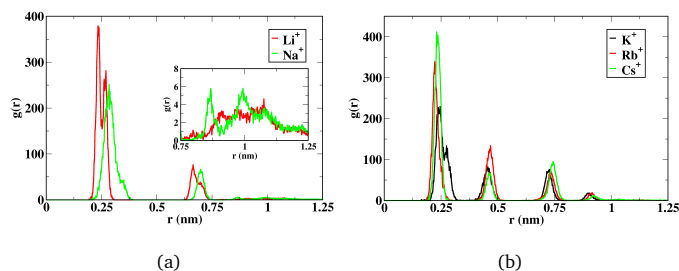


Fig. 4 U_{20} -monovalent cation RDFs. a) Li^+ , Na^+ ($r = 0.75$ to 1.25 nm shown in inset to show features) and b) K^+ , Rb^+ , Cs^+

Next, the RDFs of the monovalent and divalent cation systems were compared. The RDFs corresponding to the U_{20} - Li^+ and U_{20} - Ca^{2+} systems are shown in Figure 5a. Both Li^+ and Ca^{2+} prefer to sit inside the cluster at $r = 0.25$ nm and 0.30 nm, respectively. However, unlike the Li^+ ions, the Ca^{2+} ions do not sit on the pentagonal faces. Instead, they are bound to the cluster between $r = 0.9$ nm and 1.0 nm. In addition, the coordination number (CN) plots in Figure 5b show that the nanoclusters with divalent cations are almost fully neutralized at $r = 1.1$ nm, with just under 10 Ca^{2+} cations bound. On the other hand, nanoclusters neutralized with monovalent cations are coordinated with only 13 Li^+ at the same distance. This leaves a large uncompensated negative charge of -7 on the nanocluster neutralized with Li^+ . In summary, the nanoclusters with divalent cations are fully neutralized at a shorter distance than those with monovalent cations, which may encourage aggregation and the formation of blackberries. MD snapshots of the two systems are shown in Figure 6, which demonstrate the difference in preferred binding location.

Finally, U_{20} - H_2O RDFs were computed to understand the pre-

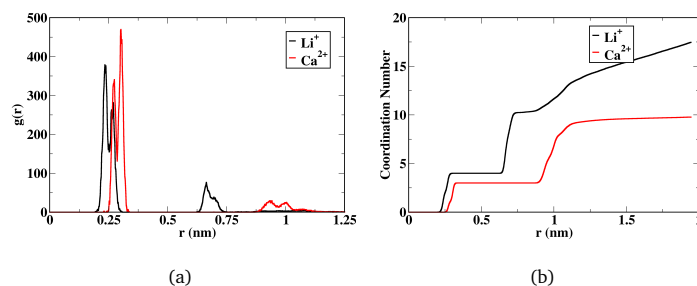


Fig. 5 Mono- vs. Divalent Cations. a) RDFs and b) CN.

ferred sites of water. The water RDFs for the Li^+ , K^+ , and Ca^{2+} systems are shown in Figure 7. The positions of the water with respect to the nanocluster do not vary based on the charge-balancing cation. In all cases, the water molecules prefer to sit in several sites within and around the nanocluster. There is a population of water molecules inside of the nanocluster that sit between $r = 0.15$ nm and 0.25 nm, the same site that cations occupy. There is a second population of water molecules inside the nanocluster located between $r = 0.42$ nm and 0.55 nm. This site is also occupied by the second group of monovalent cations (K^+ , Rb^+ , Cs^+). A final small peak of weakly associated water molecules outside the nanocluster can be found between $r = 0.85$ nm and 1.0 nm.

3.2 REMD Simulations

After computing RDFs, we wished to verify that the equilibrium distribution of cations was obtained. To better ensure equilibration, REMD was used to recompute RDF and CN plots. Figure 8 shows the RDFs and CNs computed with standard MD, compared to REMD. While the two binding sites predicted by standard MD are corroborated by the REMD simulation, there is a slight discrepancy in the relative populations. The standard MD simulation shows 4 Li^+ inside the cluster during the entire 100 ns production run, while the REMD simulation shows 4.3 Li^+ .

This fractional CN indicates fluctuations between 4 and 5 Li^+ cations inside the nanocluster, which are not seen in the standard MD simulation. Figure 9 shows the number of Li^+ cations both inside the cluster and on the outer faces over time. The number of water molecules inside of the cluster fluctuates between 8 and 12, while the number of Li^+ on the faces fluctuates between 3 and 7. The entry of a 5th Li^+ into the cluster is associated with a decrease in both the number of Li^+ on the faces and the number of water molecules inside of the nanocluster.

3.3 $\text{U}_{20}\text{-Li}^+$ Free Energy

After equilibrating the system and computing the RDFs, we wished to understand the free energy barriers that cations must surmount when moving in and out of the cluster. Without the use of REMD, only 4 Li^+ were found inside of the nanocluster for the entire 100 ns run. Starting from a configuration with 4 Li^+ cations in the nanocluster, an additional Li^+ cation was chosen randomly from the bulk and the free energy as a function of r

was computed, shown in Figure 10.

The free energy profile has minima at $r = 0.30$ and 0.65 nm. The $r = 0.30$ nm minimum corresponds to a binding site inside of the nanocluster, while the minimum at $r = 0.65$ nm corresponds to Li^+ cations sitting on the outer faces. The first minimum is split into two small minima, which manifest themselves in the RDF as two peaks (Figure 8a). For a cation to move from the bulk to one of the faces, it must overcome a 10 kJ/mol barrier, displacing another cation sitting on the face. To enter the cage, the cation must overcome a 45 kJ/mol free energy barrier. Cations that exit the cage must overcome an even larger barrier, approximately 100 kJ/mol. The free energy profile suggests that the addition of a 5th cation is spontaneous, which was confirmed by the REMD simulations. The barriers are too large to overcome within a reasonable amount of conventional MD simulation time, and therefore the use of enhanced sampling techniques was required to sample this event.

The ABF algorithm becomes numerically unstable as r approaches 0, so a lower bound was set to $r = 0.05$ nm. While the free energy profile suggests another minimum at $r = 0$, this state was completely unsampled during any of the MD simulations, even with REMD. Therefore, this state was not included in our analysis.

3.4 $\text{U}_{20}\text{-U}_{20}$ Association

Finally, we wished to explore the association of two cage clusters neutralized with monovalent and divalent cations. The free energy as a function of $\text{U}_{20}\text{-U}_{20}$ center of mass distance was computed for the $\text{U}_{20}\text{-Li}^+$ and $\text{U}_{20}\text{-Ca}^{2+}$ systems, and is shown in Figure 11. Both systems show local free energy minima at short distances. However, the free energy profiles reveal that the association of two uranyl nanoclusters neutralized with divalent Ca^{2+} is thermodynamically favorable, forming two stable states at 1.62 nm and 1.76 nm separations and binding with approximately 26 kJ/mol. On the other hand, nanoclusters neutralized with monovalent Li^+ is thermodynamically unfavorable, forming two metastable states at 1.67 and 1.77 nm, and costing approximately 6 kJ/mol of energy. The difference between the two systems is how ions are distributed radially around the cluster. As discussed previously, the nanoclusters neutralized with monovalent Li^+ cations are bound to roughly 13 cations at approximately 1 nm separation from the U_{20} center-of-mass, with the remainder of the cations freely floating around in solution. This leaves an uncompensated negative charge on the nanocluster surface, causing the nanoclusters to experience significant electrostatic repulsion when brought close to each other. On the other hand, the nanoclusters neutralized with divalent Ca^{2+} are bound to almost 10 cations at 1 nm separation, and therefore carry much less uncompensated negative charge. This reduces the electrostatic repulsion, and allows for the nanoclusters to favorably associate as they come together in the solution. In both systems, a layer of 3-4 cations and water can be found in the interstitial region in between the nanoclusters, which favorably bridges the cages together. Burns et al. found that the blackberries observed in U_{60} solutions treated with Ca^{2+} and Mg^{2+} were larger than those

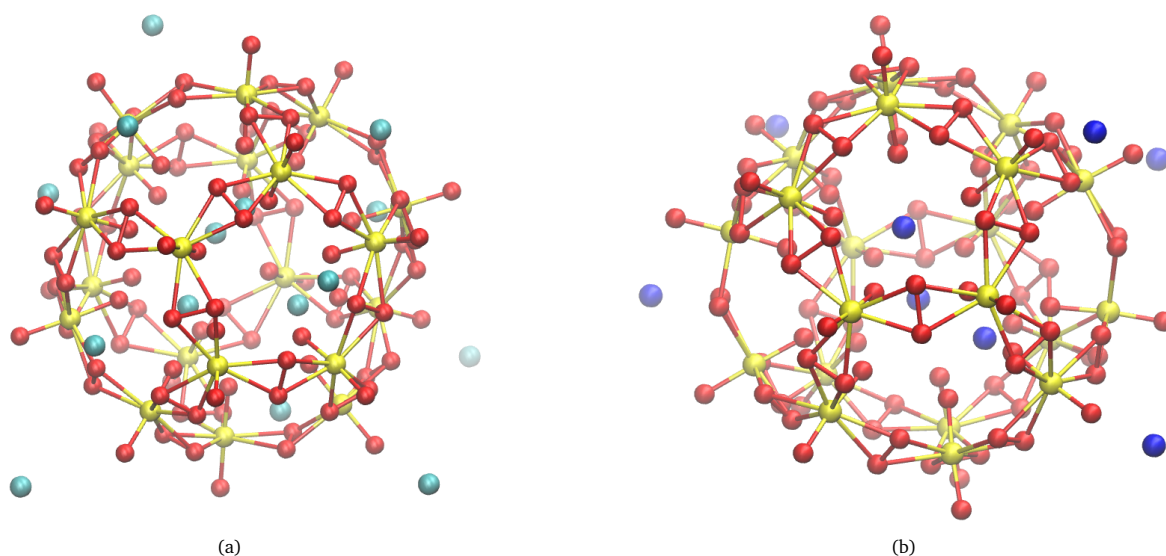


Fig. 6 Snapshots of cation populations for a) U_{20} -Li⁺ and b) U_{20} -Ca²⁺ systems. Uranium is shown as yellow, oxygen is shown as red, lithium is shown as teal, and calcium is shown as blue.

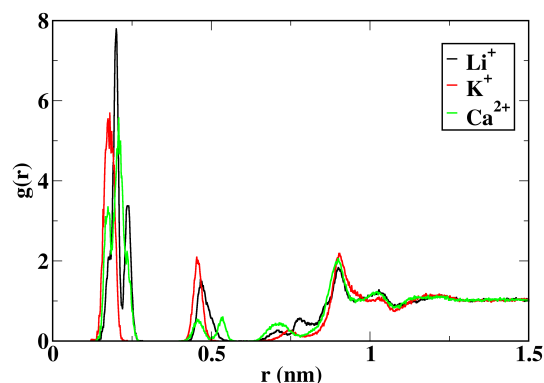


Fig. 7 U_{20} -Ow RDFs for Li⁺, K⁺, and Ca²⁺ systems.

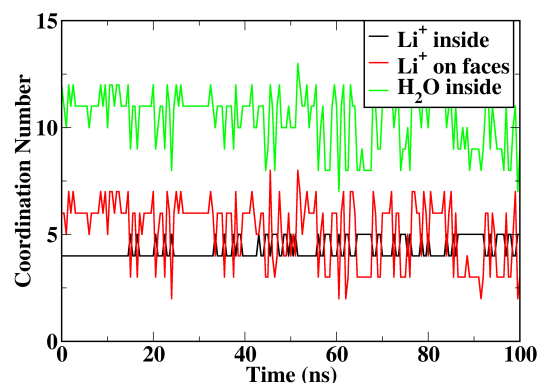


Fig. 9 The coordination of Li⁺ to the cluster over time, computed via REMD.

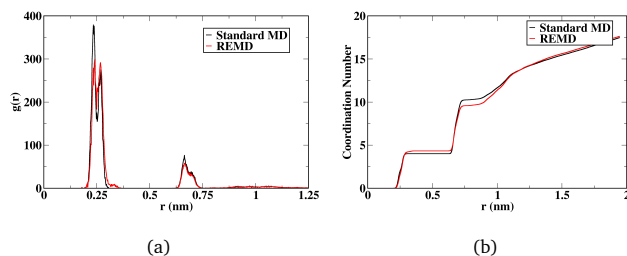


Fig. 8 Standard MD vs. REMD a) U_{20} -Li⁺ RDFs and b) U_{20} -Li⁺ CN

formed with monovalent cations.⁶ They proposed that this could be due to the fact that neutralization with divalent cations leads to a lower net surface charge, which is consistent with our calculations.

4 Conclusions

Molecular simulations were used to study uranyl peroxide nanoclusters in water. A new classical force field was parameterized from highly accurate quantum-mechanical calculations. The force field was derived to be transferable and can be used to study other uranyl nanoclusters in any solvent. The U_{20} nanocluster was modeled as a rigid body for computational efficiency and simplicity. Bonded terms should be considered in future simulations and force field development.

Previous studies on the uranyl nanoclusters were plagued by slow timescales: Miró et al. were not able to adequately determine the distribution of cations around the U_{20} nanocluster due to slow dynamics. To overcome these limitations and obtain the true equilibrium distribution of cations, this work employed REMD. Li⁺ and Na⁺ were found in two main populations: inside the cluster and on the outer faces. The larger monovalent cations,

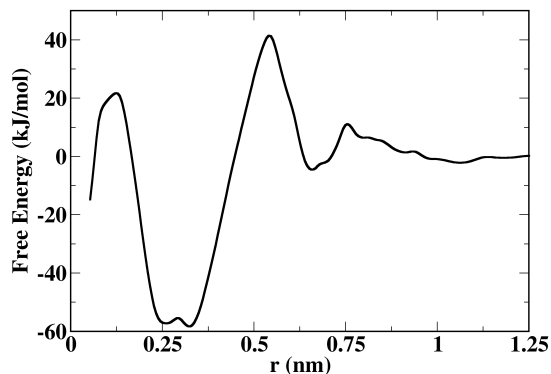


Fig. 10 Free energy as a function of U_{20} - Li^+ distance for a 5th Li^+ entering the cluster.

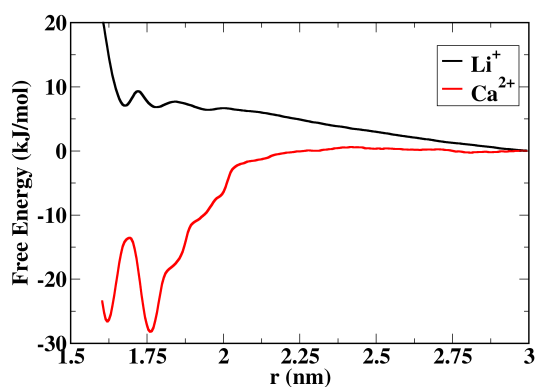


Fig. 11 U_{20} - U_{20} association free energy plots: Li^+ vs. Ca^{2+}

K^+ , Rb^+ , and Cs^+ , sit in two distinct locations inside, as well as on the outer faces. Overall, it was found that nanoclusters neutralized with monovalent cations carried a significant uncompensated negative charge while they moved through solution. On the other hand, nanoclusters neutralized with divalent cations like Ca^{2+} were almost completely neutralized in solution, with about 9 Ca^{2+} bound at all times.

The free energy associated with a Li^+ cation entering the nanocluster was computed using ABF. Li^+ cations entering the nanocluster have to surmount a 45 kJ/mol free energy barrier, and surmount a 100 kJ/mol free energy barrier to leave. Barriers of this magnitude cannot be sampled on timescales accessible to a standard simulation, so the use of REMD was warranted. A similar procedure was applied to study the association of two nanoclusters. The free energy of association was found to vary based on the valency of the cation. Nanoclusters neutralized with Li^+ carry a large negative charge as they move through solution, so the free energy increases as they are brought together. Nanoclusters neutralized with Ca^{2+} prefer to be found together, experiencing a free energy stabilization of 25 kJ/mol upon association. This provides an explanation of the difference in tertiary struc-

tures that the nanoclusters form in the presence of monovalent and divalent cations observed experimentally.

Conflicts of interest

There are no conflicts to declare.

Acknowledgements

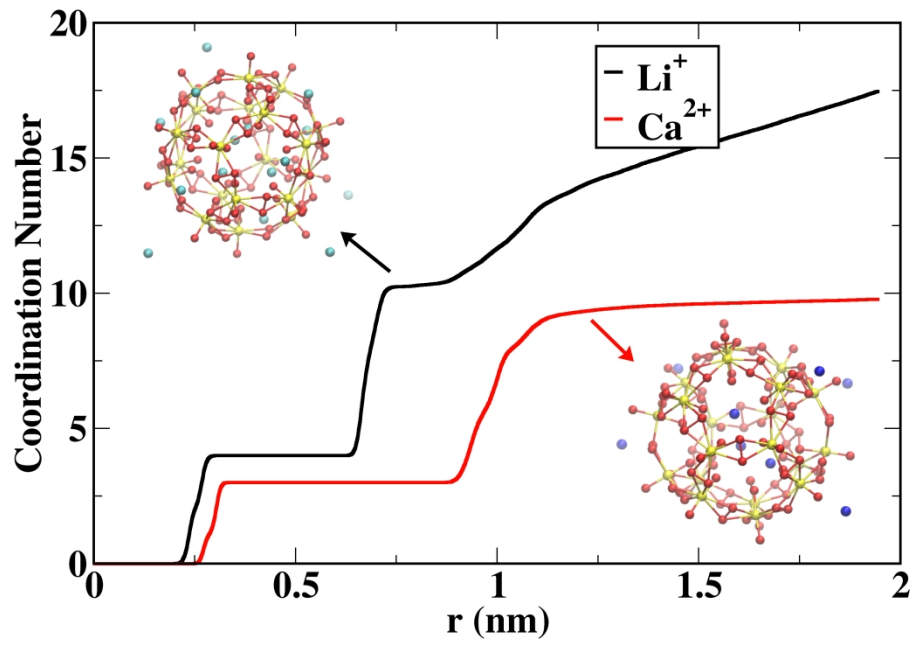
This work was supported as part of the Materials Science of Actinides Energy Frontier Research Center, funded by the U.S. Department of Energy, Office of Science, Basic Energy Sciences under award DE-SC0001089.

References

- 1 P. C. Burns, in *Actinide Polyoxometalates*, John Wiley and Sons, Inc, 2018, pp. 1–8.
- 2 P. C. Burns, *Mineral. Mag.*, 2011, **75**, 1–25.
- 3 K. A. Kubatko and P. C. Burns, *Inorg. Chem.*, 2006, **45**, 6096–8.
- 4 P. C. Burns, R. C. Ewing and F. C. Hawthorne, *Can. Mineral.*, 1997, **35**, 1551–1570.
- 5 L. J. Jouffret, S. V. Krivovichev and P. C. Burns, *Zeitschrift für Anorg. und Allg. Chemie*, 2011, **637**, 1475–1480.
- 6 J. A. Soltis, C. M. Wallace, R. L. Penn and P. C. Burns, *J. Am. Chem. Soc.*, 2016, **138**, 191–198.
- 7 K. Newcomb, S. P. Tiwari, N. Rai and E. J. Maginn, *Phys. Chem. Chem. Phys.*, 2018, **20**, 15753–15763.
- 8 S. P. Tiwari, N. Rai and E. J. Maginn, *Phys. Chem. Chem. Phys.*, 2014, **16**, 8060–8069.
- 9 P. Miró, B. Vlaisavljevich, A. L. Dzubak, S. Hu, P. C. Burns, C. J. Cramer, R. Spezia and L. Gagliardi, *J. Phys. Chem. C*, 2014, **118**, 24730–24740.
- 10 K. M. Peruski, V. Bernales, M. Dembowski, H. L. Lobeck, K. L. Pellegrini, G. E. Sigmon, S. Hickam, C. M. Wallace, J. E. S. Szymanowski, E. Balboni, L. Gagliardi and P. C. Burns, *Inorg. Chem.*, 2017, **56**, 1333–1339.
- 11 H. J. C. Berendsen, J. R. Grigera and T. P. Straatsma, *J. Phys. Chem.*, 1987, **91**, 6269–6271.
- 12 S. P. Tiwari, *PhD thesis*, University of Notre Dame, 2015.
- 13 J. Qiu and P. C. Burns, *Chemical Reviews*, 2013, **113**, 1097–1120.
- 14 F. Aquilante, L. De Vico, N. Ferré, G. Ghigo, P. Å. Malmqvist, P. Neogrady, T. B. Pedersen, M. Pitoňák, M. Reiher, B. O. Roos, L. Serrano-Andrés, M. Urban, V. Veryazov and R. Lindh, *J. Comput. Chem.*, 2010, **31**, 224–247.
- 15 B. O. Roos, R. Lindh, P.-Å. Malmqvist, V. Veryazov and P.-O. Widmark, *J. Phys. Chem. A*, 2004, **108**, 2851–2858.
- 16 B. O. Roos, R. Lindh, P.-Å. Malmqvist, V. Veryazov and P.-O. Widmark, *Chem. Phys. Lett.*, 2005, **409**, 295–299.
- 17 B. A. Hess, *Phys. Rev. A*, 1986, **33**, 3742.
- 18 M. Douglas and N. M. Kroll, *Annals of Physics*, 1974, **82**, 89–155.
- 19 F. Aquilante, T. B. Pedersen and R. Lindh, *J. Chem. Phys.*, 2007, **126**, 194106.
- 20 O. A. Vydrov and G. E. Scuseria, *J. Chem. Phys.*, 2006, **125**,

- 234109.
- 21 O. A. Vydrov, J. Heyd, A. V. Krakau and G. E. Scuseria, *J. Chem. Phys.*, 2006, **125**, 074106.
- 22 O. A. Vydrov, G. E. Scuseria and J. P. Perdew, *J. Chem. Phys.*, 2007, **126**, 154109.
- 23 M. J. Frisch, G. W. Trucks, H. B. Schlegel, G. E. Scuseria, M. A. Robb, J. R. Cheeseman, G. Scalmani, V. Barone, B. Mennucci, G. A. Petersson, H. Nakatsuji, M. Caricato, X. Li, H. P. Hratchian, A. F. Izmaylov, J. Bloino, G. Zheng, J. L. Sonnenberg, M. Hada, M. Ehara, K. Toyota, R. Fukuda, J. Hasegawa, M. Ishida, T. Nakajima, Y. Honda, O. Kitao, H. Nakai, T. Vreven, J. A. Montgomery, Jr., J. E. Peralta, F. Ogliaro, M. Bearpark, J. J. Heyd, E. Brothers, K. N. Kudin, V. N. Staroverov, R. Kobayashi, J. Normand, K. Raghavachari, A. Rendell, J. C. Burant, S. S. Iyengar, J. Tomasi, M. Cossi, N. Rega, J. M. Millam, M. Klene, J. E. Knox, J. B. Cross, V. Bakken, C. Adamo, J. Jaramillo, R. Gomperts, R. E. Stratmann, O. Yazyev, A. J. Austin, R. Cammi, C. Pomelli, J. W. Ochterski, R. L. Martin, K. Morokuma, V. G. Zakrzewski, G. A. Voth, P. Salvador, J. J. Dannenberg, S. Dapprich, A. D. Daniels, Ö. Farkas, J. B. Foresman, J. V. Ortiz, J. Cioslowski and D. J. Fox, *Gaussian 09 Revision A.1*, Gaussian Inc. Wallingford CT 2009.
- 24 W. Küchle, M. Dolg, H. Stoll and H. Preuss, *J. Chem. Phys.*, 1994, **100**, 7535–7542.
- 25 X. Cao, M. Dolg and H. Stoll, *J. Chem. Phys.*, 2003, **118**, 487–496.
- 26 X. Cao and M. Dolg, *J. Mol. Struct.: THEOCHEM*, 2004, **673**, 203–209.
- 27 R. A. Kendall, T. H. Dunning Jr and R. J. Harrison, *J. Chem. Phys.*, 1992, **96**, 6796–6806.
- 28 D. E. Woon and T. H. Dunning Jr, *J. Chem. Phys.*, 1993, **98**, 1358–1371.
- 29 A. V. Marenich, C. J. Cramer and D. G. Truhlar, *J. Phys. Chem. B*, 2009, **113**, 6378–6396.
- 30 K. Duanmu, B. Wang, A. Marenich, C. Cramer and D. Truhlar, *University of Minnesota: Minneapolis, MN*, 2015.
- 31 A. V. Marenich, S. V. Jerome, C. J. Cramer and D. G. Truhlar, *J. Chem. Theory Comput.*, 2012, **8**, 527–541.
- 32 M. P. Allen and D. J. Tildesley, *Computer Simulation of Liquids*, Clarendon Press: Oxford, 1987.
- 33 V. Pomogaev, S. P. Tiwari, N. Rai, G. S. Goff, W. Runde, W. F. Schneider and E. J. Maginn, *Phys. Chem. Chem. Phys.*, 2013, **15**, 15954–63.
- 34 I. S. Joung and T. E. Cheatham, *J. Phys. Chem. B*, 2008, **112**, 9020–9041.
- 35 S. Mamatkulov, M. Fyta and R. R. Netz, *J. Chem. Phys.*, 2013.
- 36 M. J. Abraham, T. Murtola, R. Schulz, S. Páll, J. C. Smith, B. Hess and E. Lindahl, *SoftwareX*, 2015, **1**, 19–25.
- 37 K. Hukushima and K. Nemoto, *J. Phys. Soc. Jpn.*, 1996, **65**, 1604–1608.
- 38 Y. Sugita and Y. Okamoto, *Chem. Phys. Lett.*, 1999, **314**, 141–151.
- 39 D. Van Der Spoel and M. M. Seibert, *Phys. Rev. Lett.*, 2006, **96**, 1–4.
- 40 D. Frenkel and B. Smit, *Understanding Molecular Simulation From Algorithms to Applications*, Academic Press, New York, 2002.
- 41 E. Darve, D. Rodríguez-Gómez and A. Pohorille, *J. Chem. Phys.*, 2008, **128**, 1–13.
- 42 H. Sidky, Y. J. Colón, J. Helfferich, B. J. Sikora, C. Bezik, W. Chu, F. Giberti, A. Z. Guo, X. Jiang, J. Lequieu, J. Li, J. Moller, M. J. Quevillon, M. Rahimi, H. Ramezani-Dakhel, V. S. Rathee, D. R. Reid, E. Sevgen, V. Thapar, M. A. Webb, J. K. Whitmer and J. J. de Pablo, *J. Chem. Phys.*, 2018, **148**, 44104.

The aggregation of uranyl nanoclusters is investigated with molecular dynamics simulations.



1164x899mm (72 x 72 DPI)